Data Repository materials.

1. Methods.

a. Determination of layer orientations. 1m-resolution stereo terrain models were produced from High-Resolution Imaging Science Experiment (HiRISE) images, using the method of Kirk et al. (2008), and best-fitting planar layer orientations were calculated via linear regression of points along bedding contacts (procedure of Lewis et al., 2006). To confirm that our procedure is measuring layers within the mound, and is not biased by surficial weathering textures nor by the present-day slope, we made measurements around a small reentrant canyon incised into the SW corner of the Gale mound. Within this canyon, present-day slope dip direction varies through 360°, but as expected the measured layer orientations dip consistently (to the W).

b. MarsWRF simulations of Gale Crater. MarsWRF (Toigo et al., 2012) is the Mars version of planetWRF (Richardson et al., 2007), an extension of the widely-used Weather Research and Forecasting model. To produce the wind analysis shown in Figure DR1, MarsWRF was run as a global model at 2° resolution, with three increasingly high-resolution domains “nested” over Gale Crater to increase the resolution there to ~4 km. Each nested domain is both driven by its parent domain, and feeds information back to the parent domain, while also responding to surface variations (e.g. topography, albedo) at the higher resolution of the nest.

c. Assessment of alternative mechanisms for producing outward dips. Few geologic processes can produce primary outward dips of (3±2)° (Figures 1, 2). Spring mounds lack laterally continuous marker beds of the >10 km extent observed (Anderson & Bell, 2010). Preferential dissolution, landsliding/halotectonics, post-impact mantle rebound, and lower-crustal flow can lead to postdepositional outward tilting. On Early Mars, isostatic compensation timescales are $<<10^6$ yr. In order for postdepositional mantle rebound to produce outward tilts, the mound must have accumulated at implausibly fast rates. Mars' crust is constrained to be $\lesssim$90 km thick at Gale's location (Nimmo & Stevenson, 2001), so lower-crustal flow beneath 155km-diameter Gale would have a geometry that would relax Gale Crater from the outside in, incompatible with simple outward tilting. Additionally, Gale is incompletely compensated (Konopliv et al., 2011) and postdates dichotomy-boundary faulting, so Gale postdates the era when Mars' lithosphere was warm enough for crustal flow to relax the dichotomy boundary and cause major deformation (Irwin & Watters, 2010). Any tectonic mechanism for the outward dips would correspond to ~3-4 km of floor uplift of originally horizontal layers. This is comparable to the depth of a fresh crater of this size and inconsistent with the current depth of the southern (mound-free) half of the crater if we make the reasonable approximation that wind cannot quickly erode basalt. Tectonic doming would put the mound's upper surface into extension and produce extensional faults (e.g., p.156 in Melosh, 2011), but these are not observed. Preferential dissolution leaves karstic depressions (Hovorka, 2000), which are not observed at Gale. Landsliding/halotectonics can produce deformed beds in layered sediments on Earth and Mars (e.g. Metz et al., 2010, Hudec & Jackson 2011). These sites show order-unity strain and contorted bedding, but the layers near the base of the mound show no evidence for large strains at kilometer scale, except for a possible late-stage landslide on the mound's north flank (Anderson & Bell, 2010).

d. Scaling sediment transport. Conservation of sediment (Anderson, 2008) in the atmospheric boundary-layer can be written as:

$$\mathrm{d}z/\mathrm{d}t = D - E = CWs - E$$

Here C is volumetric sediment concentration, W_s is settling velocity, and E is the rate of sediment pick-up from the bed. In aeolian transport of dry sand and alluvial-river transport, induration processes are weak or absent and so the bed has negligible intergrain cohesion. C tends to E/W_s over a saturation length scale that is inversely proportional to W_s (for $dz/dt > 0$) or E (for $dz/dt < 0$). This scale is typically short, e.g. ~1-20m, for the case of a saltating sand on Earth (Kok et al., 2012). Our simplifying assumption that $D \neq f(x)$ and therefore $C \neq f(x)$ implies that this saturation length scale is large compared to the morphodynamic feedback of interest. For the case of net deposition ($dz/dt > 0$) this could correspond to settling-out of sediment stirred up by dust storms (e.g. Vaughan et al., 2010). These events have characteristic length scales $>10^2$ km (Szwast et al., 2006), larger than the scale of Gale's mound and justifying the approximation of uniform D. For the case of net erosion ($dz/dt < 0$), small E implies a detachment-limited system where sediment has some cohesion. The necessary degree of induration is not large: for example, 6-10 mg/g chloride salt increases the threshold wind stress for saltation by a factor of e (Nickling, 1984). Fluid pressure alone cannot abrade the bed, and the gain in entrained-particle mass from particle impact equals the abrasion susceptibility, $\sim 2 \times 10^{-6}$ for basalt under modern Mars conditions (Bridges et al., 2012) and generally <<1 for cohesive materials, preventing runaway adjustment of C to E/W_s. Detachment-limited erosion is clearly appropriate for slope-wind erosion on modern Mars (because sediment mounds form yardangs and shed boulders, indicating that they are cohesive/indurated), and is probably a better approximation to ancient erosion processes than transport-limitation (given the evidence for ancient shallow diagenesis, and soil crusts; e.g., McLennan & Grotzinger, 2008).

e. Reference parameter choices. Coriolis forces are neglected because almost all sedimentary rock mounds on Mars are equatorial (Kite et al., 2012). Additional numerical diffusivity at the 10^{-3} level is used to stabilize the solution. Analytic and experimental results show that in slope-wind dominated landscapes, the strongest winds occur close to the steepest slopes (Manins & Sarford, 1987). *L* will vary across Mars because of 3D topographic effects, and will vary in time because of changing atmospheric density. Ye et al. (1990) find $L \sim$ 20km for Mars slopes with negligible geostrophic effects, and Eq. 49 in Magalhaes & Gierasch (1982) gives $L \sim$ 25 km for Gale-relevant slopes. Simulations of gentle Mars slope winds strongly affected by planetary rotation suggest $L \sim$ 50-100 km (e.g., Savijärvi & Siili, 1993). Entrainment acts as a drag coefficient, ~0.02-0.05 for Gale-relevant slopes (e.g. Horst & Doran, 1986**)**, suggesting L = 20-50 km for a 1km-thick cold boundary layer. Therefore we take $L \sim 10^{1-2}$ km to be reasonable, but with the expectation of significant *L/R* variability, explored in the next section.

2. Sensitivity tests: controls on mound growth and form. To confirm that our results do not depend on idiosyncratic parameter choices, we carried out a parameter sweep in α, *D'*, and *R/L* (Figure DR2). Weak slope dependence (α = 0.05) is sufficient to produce strata that dip toward the foot of the crater/canyon slope (like a sombrero hat). Similarly weak *negative* slope dependence (α = -0.05) is sufficient to produce concave-up fill. At low *R/L* (i.e., small craters) or at low α, *D'* controls overall mound shape and slope winds are unimportant. When *D'* is high, layers fill the crater; when *D'* is low, layers do not accumulate. When either α or *R/L* or both are $\gtrsim$1, slope-wind enhanced erosion and transport dominates the behavior. Thin layered crater floor deposits form at low *D'*, and large mounds at high *D'*. If *L* is approximated as being constant across the planet, then *R/L* is proportional to crater/canyon size. There is net aggradation everywhere for small *R/L*, although a small moat can form as a result of relatively low net aggradation near the crater wall. For larger *R/L*, moats form, and for the largest craters/canyons, multiple mounds can form eventually because slope winds break up the deposits. This is consistent with data, which suggest a maximum length scale for mounds (Figure DR3). Small exhumed craters in Meridiani show concentric layering consistent with concave-up dips. Larger Meridiani craters, together with the north polar ice mounds, show a simple single mound. Gale and Nicholson Craters, together with the smaller Valles Marineris chasmata, show a single mound with an undulating top. The largest canyon system on Mars (Ophir-Candor-Melas) shows multiple mounds per canyon. Gale-like mounds (with erosion at both toe and the summit) are most likely for high R/L, high α, and intermediate D' (high enough for some accumulation, not so high as to fill the crater; Figure DR2).

U_o is set to zero in Figure 3. Sensitivity tests show that for a given D', varying U_o has little effect on the pattern of erosion because spatial variations are still controlled by slope winds. Equation (3) implies the approximation $E \sim \max(U)^{\alpha} \sim \sum \mathrm{U}^{\alpha}$, which is true as $\alpha \rightarrow \infty$. To check that this approximation does not affect conclusions for α = 3-4 (Kok et al., 2012), we ran a parameter sweep with $E \sim (U_+^{\alpha} + U_-^{\alpha})$. For nominal parameters (Figure 3), this leads to only minor changes in mound structure and stratigraphy (e.g., 6% reduction in mound height and <1% in mound width at late time). For the parameter sweep as a whole, the change leads to a slight widening of the regions where the mound does not nucleate or overspills the crater (changing the outcome of 7 out of the 117 cases shown in Figure DR2). The approximation would be further supported if (as is likely) there is a threshold U below which erosion does not occur. If MSL shows that persistent snow or ice was needed as a water source for layer cementation (Niles & Michalski, 2009; Kite et al., 2012), then additional terms will be required to track humidity and the drying effect of föhn winds (e.g. Madeleine et al., 2012).

These sensitivity tests suggest that mounds are a generic outcome of steady uniform deposition modified by slope-wind enhanced erosion and transport for reasonable Early Mars parameter values.

Data Repository References

Anderson, R.S., 2008, The Little Book of Geomorphology: Exercising the Principle of Conservation, http://instaar.colorado.edu/~andersrs/The_little_book_010708_web.pdf

Horst, T. W., & Doran, J. C., 1986, Nocturnal drainage flow on simple slopes. *Boundary-Layer Meteorol.* 34, p. 263-286.

Hovorka, S. D., 2000, Understanding the processes of salt dissolution and subsidence in sinkholes and unusual subsidence over solution mined caverns and salt and potash mines, Technical Session: Solution Mining Research Institute Fall Meeting, p. 12–23, downloaded from http://www.beg.utexas.edu/environqlty/pdfs/hovorka-salt.pdf

Hudec, M.R., & Jackson, M.P.A., 2011, The salt mine : a digital atlas of salt tectonics. Austin, Tex: Jackson School of Geosciences, University of Texas at Austin.

Irwin, R. P., III, and T. R. Watters, 2010, Geology of the Martian crustal dichotomy boundary, *J. Geophys. Res*. 115, E11006, doi:10.1029/2010JE003658.

Konopliv, A.S. et al., 2011, Mars high resolution gravity fields from MRO, Mars seasonal gravity, and other dynamical parameters, *Icarus* 211, p. 401-428.

Madeleine, J.-B., Head, J. W., Spiga, A., Dickson, J. L., & Forget, F., 2012, A study of ice accumulation and stability in Martian craters under past orbital conditions using the LMD mesoscale model, *Lunar and Planet. Sci. Conf*. 43, abstract no. 1664.

Magalhaes, J., & Gierasch, P., 1982, A model of Martian slope winds: Implications for eolian transport, *J. Geophys. Res.* 87, p. 9975-9984.

Manins, P. C., & Sawford, B. L.,1987, A model of katabatic winds, *J. Atmos. Sci.* 36, 619-630.

Metz, J., Grotzinger, J., Okubo, C., & Milliken, R., 2010, Thin-skinned deformation of sedimentary rocks in Valles Marineris, Mars*, J. Geophys. Res*. 115, E11004.

Melosh, H.J., 2011, Planetary Surface Processes, Cambridge University Press.

Nickling, W.G., 1984, The stabilizing role of bonding agents on the entrainment of sediment by wind. *Sedimentology* 31, 111-117. doi: 10.1111/j.1365-3091.1984.tb00726.x.

Nimmo, F., and Stevenson, D.J. 2001, Estimates of Martian crustal thickness from viscous relaxation of topography, *J. Geophys. Res*. 106, 5085-5098, doi:10.1029/2000JE001331.

Richardson, M.I., Toigo, A.D., and Newman, C.E., 2007, PlanetWRF: A general purpose, local to global numerical model for planetary atmospheric and climate dynamics, *J. Geophys. Res.* 112, E09001.

Szwast, M., Richardson, M. and Vasavada, A., 2006, Surface dust redistribution on Mars as observed by the Mars Global Surveyor and Viking orbiters. *J. Geophys. Res*. 111, E11008.

Savijärvi, H., and Siili, T., 1993, The Martian slope winds and the nocturnal PBL jet. *J. Atmos. Sci.* 50, p. 77-88.

Vaughan, A.F., et al., 2010. Pancam and Microscopic Imager observations of dust on the Spirit Rover: Cleaning events, spectral properties, and aggregates, *Mars* 5, p. 129-145.

Ye, Z.J., Segal, M., & Pielke, R.A., 1990, A comparative study of daytime thermally induced upslope flow on Mars and Earth. *J. Atmos. Sci.* 47, p. 612-628.

Data Repository Table 1: Layer orientation measurements

Lat	Lon	Z (m)	Dip (°)	Dip Az (°)	HiRISE Image ID
-5.022347	138.394900	-3263.1	3.53	30.68	PSP_008437_1750
-5.023877	138.392660	-3201.9	2.52	62.01	PSP_008437_1750
-5.015876	138.386310	-3216.9	2.1	94.68	PSP_008437_1750
-5.015508	138.387020	-3201.4	7.31	41.72	PSP_008437_1750
-4.998358	138.391680	-3554.2	2.06	54.81	PSP_008437_1750
-5.003035	138.387800	-3429.9	0.43	-21.29	PSP_008437_1750
-5.004517	138.379910	-3425.8	5.04	89.54	PSP_008437_1750
-5.004179	138.379580	-3434.5	3.79	70.24	PSP_008437_1750
-4.997492	138.392530	-3583.8	4.65	51.98	PSP_008437_1750
-5.012374	138.396710	-3421.5	4.14	47.28	PSP_008437_1750
-5.031424	138.395590	-3290.1	4.07	40.92	PSP_008437_1750
-5.030106	138.396180	-3308.2	2.55	76.18	PSP_008437_1750
-5.03171	138.393740	-3260.1	3.24	43.31	PSP_008437_1750
-5.035189	138.392050	-3176.3	2.07	75.25	PSP_008437_1750
-5.035062	138.391700	-3173.3	2.21	86.77	PSP_008437_1750
-4.685812	137.494850	-4098.5	3.34	148.1	ESP_023957_1755
-4.684778	137.491970	-4103.8	3.98	174.47	ESP_023957_1755
-4.689331	137.480520	-4101.3	6.06	132.82	ESP_023957_1755
-4.659387	137.533150	-4120.3	6.48	114.03	ESP_023957_1755
-4.65886	137.537400	-4108.2	0.5	13.56	ESP_023957_1755
-4.662119	137.535520	-4073.1	3.9	-149.05	ESP_023957_1755
-4.664102	137.525670	-4127.1	7.16	130.19	ESP_023957_1755
-4.663656	137.524870	-4138.3	4.83	152.05	ESP_023957_1755
-4.665528	137.526530	-4101.2	4.59	-153.08	ESP_023957_1755
-4.676802	137.506150	-4083.2	2.32	83.97	ESP_023957_1755
-4.672137	137.510280	-4128	3.24	91.62	ESP_023957_1755
-4.871501	137.270980	-3849.6	1.09	10.19	PSP_001488_1750
-4.871837	137.266710	-3857.7	5.19	85.97	PSP_001488_1750
-4.872691	137.270730	-3833.2	2.61	-51.44	PSP_001488_1750
-4.917952	137.284340	-3513.9	6.78	136.55	PSP_001488_1750
-4.831027	137.330630	-3768.9	2.16	140.09	PSP_001488_1750
-4.828565	137.330360	-3792.5	2.65	143.84	PSP_001488_1750
-4.846642	137.303380	-3802.8	4.38	124.94	PSP_001488_1750
-4.845724	137.303070	-3815.7	4.51	111.27	PSP_001488_1750
-4.845501	137.304420	-3799.2	2.34	79.11	PSP_001488_1750
-4.863885	137.332420	-3507.1	2.04	132.56	PSP_001488_1750
-4.93696	137.311640	-3278.4	3.74	129.01	PSP_001488_1750
-4.938936	137.309840	-3287.6	4.46	119.79	PSP_001488_1750
-4.920126	137.322160	-3290.9	1.79	134.69	PSP_001488_1750
-4.922859	137.317020	-3306.6	4.2	160.7	PSP_001488_1750
-4.901912	137.338220	-3265.6	4.87	-174.83	PSP_001488_1750

-4.892401	137.332800	-3389.9	6.71	117.93	PSP_001488_1750
-4.863151	137.342100	-3464.4	5.66	105.35	PSP_001488_1750
-4.779928	137.409690	-3656.9	3.69	167.09	PSP_009149_1750
-4.777029	137.405330	-3736.8	2.13	168.14	PSP_009149_1750
-4.75303	137.438670	-3810.7	6.07	128.67	PSP_009149_1750
-4.752131	137.438100	-3823.7	5.92	123.62	PSP_009149_1750
-5.348423	137.227120	-2745.9	2.68	154.47	ESP_012907_1745
-5.348098	137.227470	-2757.1	2.32	144.88	ESP_012907_1745
-5.341016	137.209820	-2891.2	2.58	135.34	ESP_012907_1745
-5.337968	137.210930	-2796.8	4.54	151.03	ESP_012907_1745
-5.377012	137.207730	-2879.1	1.63	165.41	ESP_012907_1745
-5.384663	137.190610	-3005.3	4.73	156.7	ESP_012907_1745
-5.413138	137.185680	-2848.5	4.57	133.72	ESP_012907_1745
-5.40772	137.197850	-2779.3	4.05	158.01	ESP_012907_1745
-5.392686	137.208330	-2756.1	10.83	163.21	ESP_012907_1745
-5.371398	137.174520	-3359.7	6.02	159.19	ESP_012907_1745
-5.342561	137.176890	-3130.9	6.76	160.11	ESP_012907_1745
-5.458482	137.183800	-2752.8	2.49	142.76	ESP_012907_1745
-5.459221	137.188840	-2674.5	3.58	162.7	ESP_012907_1745
-5.460307	137.188440	-2696.5	3.97	166.94	ESP_012907_1745
-5.392535	137.196770	-2848.2	2.48	170.27	ESP_012907_1745
-5.390379	137.195930	-2898.2	3.04	156.57	ESP_012907_1745
-5.390219	137.191070	-2988.8	2.6	144.9	ESP_012907_1745
-5.411481	137.194250	-2811.9	2.09	146.02	ESP_012907_1745
-5.623904	138.328080	-2971.2	1.74	-43.56	ESP_014186_1745
-5.627848	138.337550	-3000.2	2.17	-71.76	ESP_014186_1745
-5.598681	138.339300	-2856.2	1.26	116.18	ESP_014186_1745
-5.584488	138.338620	-2705.9	2.25	-69.68	ESP_014186_1745
-5.584654	138.354940	-2710	2.45	-82.66	ESP_014186_1745
-5.605716	138.360870	-2907.7	0.3	-175.97	ESP_014186_1745
-5.570108	138.366460	-2674.6	5.23	-61.61	ESP_014186_1745
-5.572424	138.360000	-2589.6	2.17	-86.77	ESP_014186_1745
-5.588566	138.326250	-2685.2	2.6	-27.67	ESP_014186_1745
-5.580666	138.333270	-2681.5	1.76	-81.46	ESP_014186_1745
-5.534321	138.325470	-2424.8	4.35	-117.38	ESP_014186_1745
-5.542813	138.327860	-2454.8	3.37	-104.06	ESP_014186_1745
-5.573589	138.289520	-2658.6	2.2	-115.72	ESP_014186_1745
-5.566658	138.288200	-2644.4	1.15	74.46	ESP_014186_1745
-5.581102	138.309950	-2667.3	1.06	-65.97	ESP_014186_1745

Data Repository Figure Captions

Figure DR1. Annual maximum wind speed (m/s) within Gale Crater from MarsWRF simulations, showing that the strongest winds within the crater are associated with steep slopes. Black topography contours are spaced at 500m intervals. The winds are extrapolated to 1.5m above the surface using boundary layer similarity theory (the lowest model layer is at ~9m above the surface).

Figure DR2. Overall growth and form of sedimentary mounds – results from a model parameter sweep varying *R/L* and *D′*, with fixed $\alpha = 3$. Black square corresponds to the results shown in more detail in Figure 3. Symbols correspond to the overall results:– no net accumulation of sediment anywhere (blue open circles); sediment overtops crater/canyon (red filled circles); mound forms and remains within crater (green symbols). Green filled circles correspond to outcomes where layers are exposed at both the toe and the summit of mound, similar to Gale.

Figure DR3. Width of largest mound does not keep pace with increasing crater/canyon width, suggesting a length threshold beyond which slope winds break up mounds. Blue dots correspond to nonpolar crater data, red squares correspond to canyon data, and green dots correspond to polar ice mound data. Gray vertical lines show range of uncertainty in largest-mound width for Valles Marineris canyons. Blue dot adjacent to "G" corresponds to Gale Crater. Craters smaller than 10km were measured using Context Camera (CTX) or HiRISE images. All other craters, canyons and mounds were measured using the Thermal Emission Imaging System (THEMIS) global day infrared mosaic on a Mars Orbiter Laser Altimeter (MOLA) base. Width is defined as polygon area divided by the longest straight-line length that can be contained within that polygon.

Figure DR1

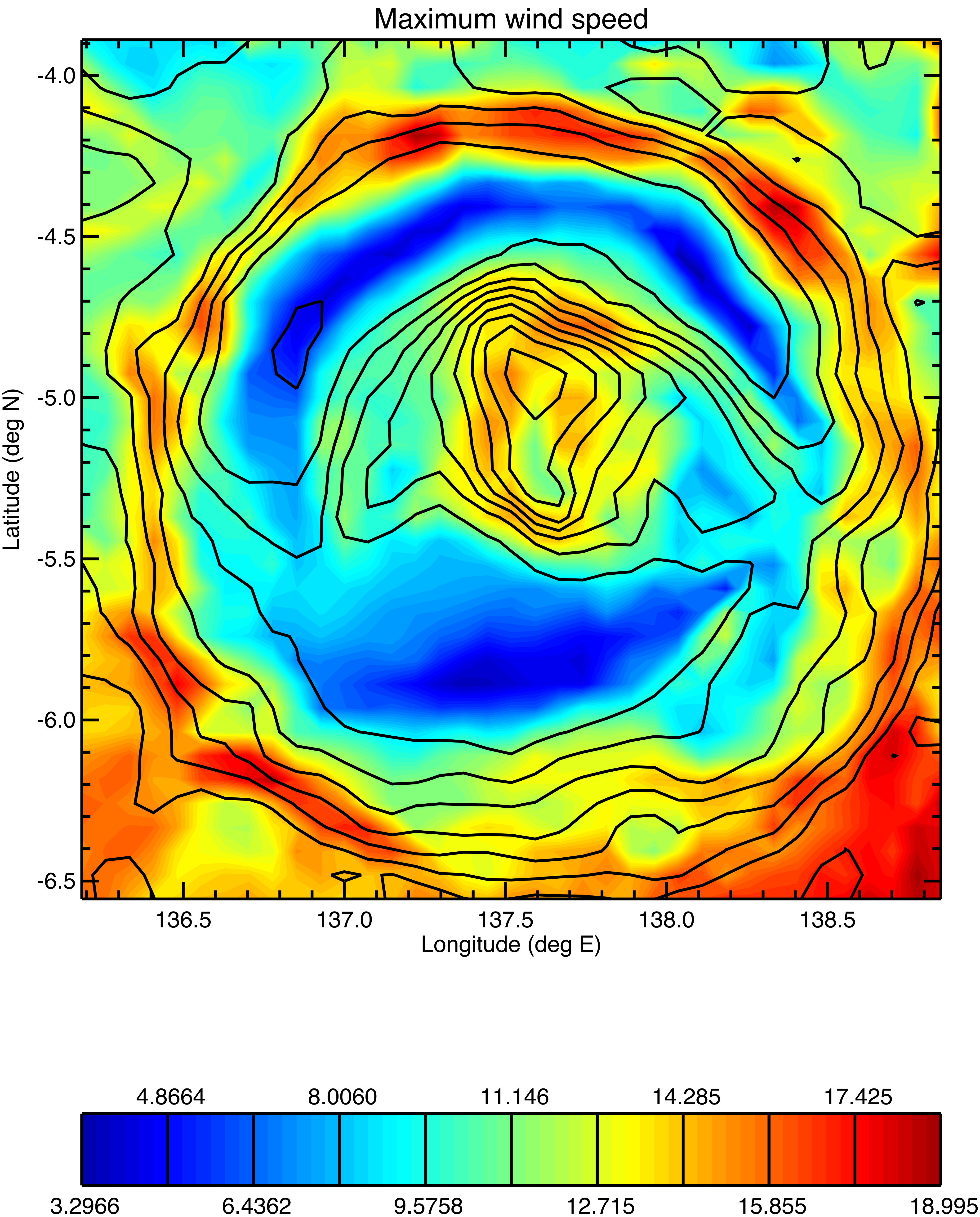

Maximum wind speed
-4.0
-4.5
-5.0
-5.5
-6.0
-6.5
Latitude (deg N)
136.5
137.0
137.5
138.0
138.5
Longitude (deg E)
4.8664
8.0060
11.146
14.285
17.425
3.2966
6.4362
9.5758
12.715
15.855
18.995

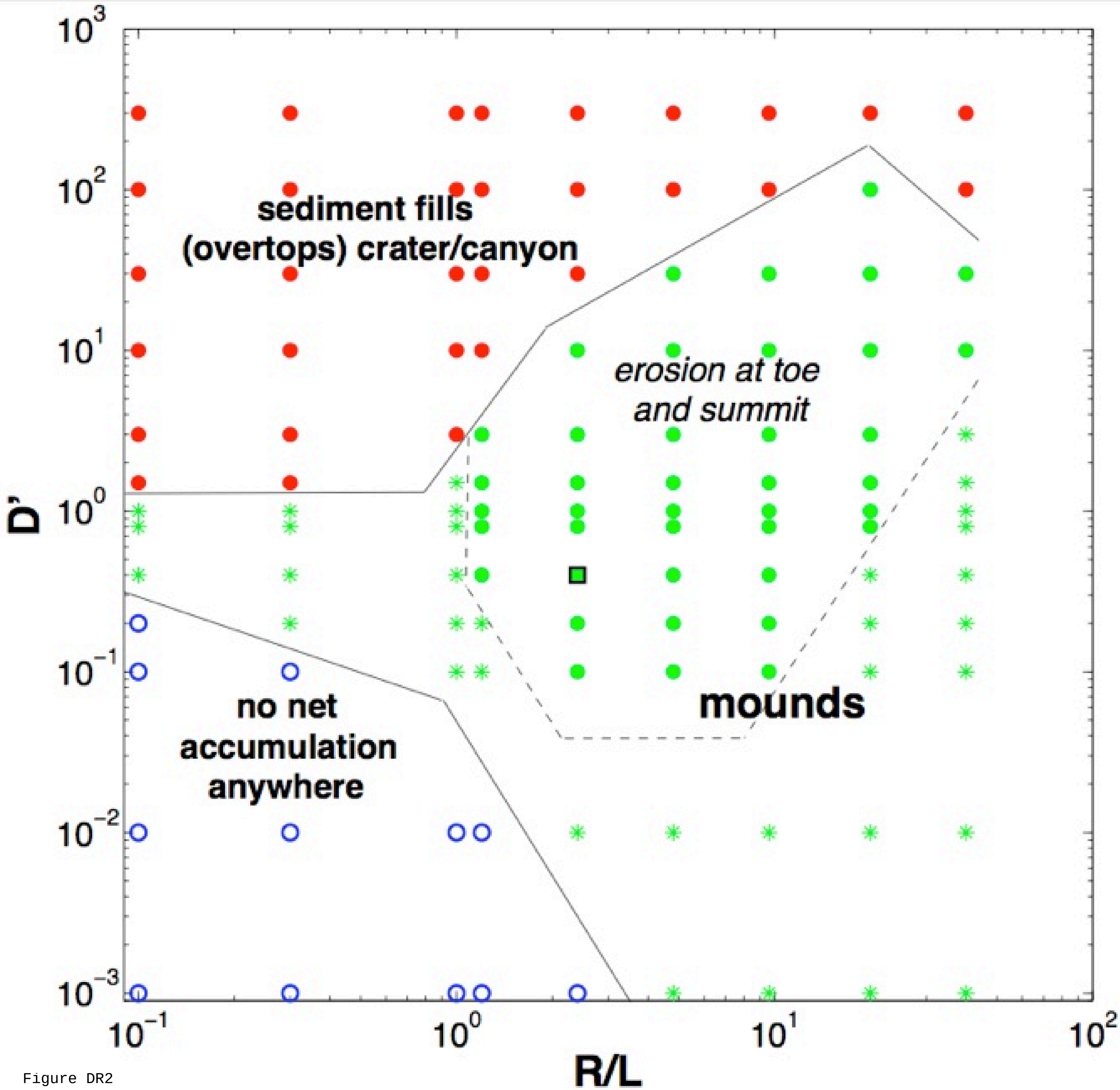

sediment fills
(overtops) crater/canyon
erosion at toe
and summit
mounds
no net
accumulation
anywhere
D'
R/L
10^{3}
10^{2}
10^{1}
10^{0}
10^{-1}
10^{-2}
10^{-3}

Figure DR2

Figure DR3

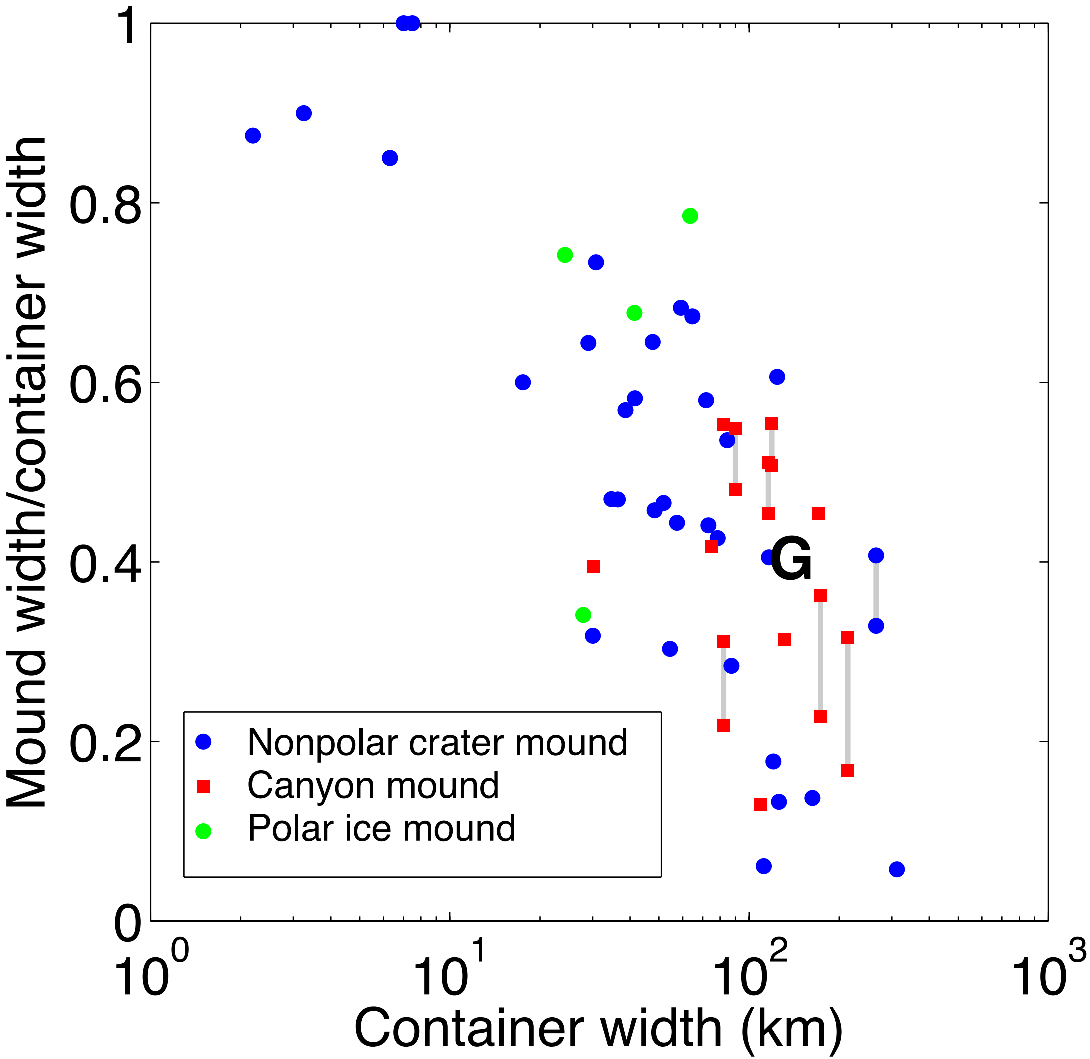

1
0.8
0.6
0.4
0.2
0
Mound width/container width
10^0
10^1
10^2
10^3
Container width (km)
G
Nonpolar crater mound
Canyon mound
Polar ice mound